Rashba–Edelstein Effect in the h-BN Van Der Waals Interface for Magnetization Switching

Qidong Xie, Weinan Lin, Jinghua Liang, Hengan Zhou, Moaz Waqar, Ming Lin, Siew Lang Teo, Hao Chen, Xiufang Lu, Xinyu Shu, et al.

Rashba-Edelstein effect in the h-BN van der Waals interface for magnetization switching

Qidong Xie[1,†], Weinan Lin[1,†], Jinghua Liang[2], Hengan Zhou[3], Moaz Waqar[1,4], Hao Chen[5], Xiufang Lu[5], Xinyu Shu[1], Liang Liu[1], Shaohai Chen[1], Chenghang Zhou[1], Jianwei Chai[6], Ping Yang[1,7], Kian Ping Loh[5], John Wang[1], Wanjun Jiang[3], Aurelien Manchon[8,], Hongxin Yang[2,*], Jingsheng Chen[1,*]*

1. Department of Materials Science and Engineering, National University of Singapore, 117575, Singapore

2. Ningbo Institute of Materials Technology and Engineering, Chinese Academy of Sciences, Ningbo 315201, China; Center of Materials Science and Optoelectronics Engineering, University of Chinese Academy of Sciences, Beijing 100049, China

3. State Key Laboratory of Low-Dimensional Quantum Physics and Department of Physics, Tsinghua University, Beijing 100084, China

4. NUS Graduate School for Integrative Sciences and Engineering, National University of Singapore 119077, Singapore

5. Department of chemistry, National University of Singapore, 117543, Singapore

*6. Department of Electronic Material Institute of Material Research and Engineering A*STAR Singapore 138634, Singapore*

7. Singapore Synchrotron Light Source (SSLS), National University of Singapore, 5 Research Link, 117603, Singapore

8. Aix-Marseille Univ, CNRS, CINaM, Marseille, France

[†]These authors contributed equally to this work.

Coresponding authors:

Prof. Jingsheng Chen

Email: msecj@nus.edu.sg

Prof. Hongxin Yang

Email: hongxin.yang@nimte.ac.cn

Prof. Aurelien Manchon

Email: aurelien.manchon@univ-amu.fr

Current induced spin-orbit torque (SOT) offers an electrical way to control the magnetic state[1,2], which is promising for future low-power spintronics. In general, the SOT originates from spin Hall effect (SHE) in heavy metals[3], and/or Rashba-Edelstein effect (REE) in interfaces or structures without inversion symmetry[4]. The REE-induced SOT relies on the Rashba spin-orbit coupling (SOC) in the studied structure, which enables the electric-field tunability on spin-orbit effective fields and thus attracts great interests[5–7]. However, the unambiguous demonstration of the REE-SOT induced magnetization switching and its electric-field tunability is still lacking. Here, we demonstrate the REE-SOT induced magnetization switching in a h-BN/$SrRuO_3$ bilayer structure. The insulating h-BN unexpectedly induces a giant Rashba effect at the van der Waals interface with a perpendicular magnetized $SrRuO_3$ $(110)_{pc}$ thin film, which is supported by our first-principles calculations. In addition, a simplified tight-binding model is built to explain the origin of the SOT. Furthermore, modulation of the current-induced SOT and magnetization switching by an electric field have been successfully achieved via ionic-liquid gating experiment. Our study paves the way for exploring the current-induced SOT and magnetization switching by integrating van der Waals materials with the functional ferromagnets.

The electric field tunability on the current-induced SOT not only gives rise to an extra degree of freedom for electrically manipulating the magnetizations for devices application, but

also provide a powerful method for fundamental studies. In a conventional heavy metal (HM)/ferromagnetic metal (FM)/oxide tri-layers structure, the current-induced SOTs are considered to be mainly due to the SHE from the bulk HM, which has a very small screening length and thus makes the directly electrostatic effect trivial[8]. Consequently, a sizable modulation of the SOTs can only be achieved via electric-field driven motion of oxygen at the interface between the oxide layer and ferromagnetic metal (FM)[9], which strongly influences the magnetic anisotropy of FM simultaneously. Compared to the SHE-induced SOT, the modulation of REE-induced SOT is more straightforward and desirable, thanks to the essential role of the Rashba effect, whose strength is related to the potential difference that the involving charge electrons experience. Indeed, there are a few works reporting the tunable REE-induced spin-orbit effective field in structures like $SrTiO_3$-based heterostructures[5,6], ferroelectric/metal interface[10,11] and Fe/GaAs interface[7]. However, the REE in these structures has not been demonstrated to have the ability to drive magnetization switch by applying a charge current. Furthermore, whether the electric field effect on the REE-induced SOT can be transferred to the tuning capability on the current-induced magnetization switching remains unexplored. These might be achieved by searching appropriate material systems which host significant REE and FM layer with perpendicular magnetic anisotropy (PMA) simultaneously.

On the other hand, to date, SOTs have been mostly demonstrated in transition metals[1,2,12,13] and van der Waals materials[14–16] which possess strong SOC and act as a source of spin current and torques. In order to boost the torque efficiency, one strategy is to exploit a topological insulator as a spin source layer, rather than a heavy metal. In this situation, the current is expected to mostly flow at the interface with the ferromagnet and generate extremely efficient torques. However, the difficulty to grow truly insulating topological insulator limits the applicability of this approach and strategies exploiting sputtered topological compounds are currently being explored[17]. Alternatively, it has been proposed to use light elements such

as graphene to enhance the interfacial potential drop[18]. The cooperation between the enhanced interfacial electric field and the atomic SOC of the ferromagnetic layer results in large Rashba SOC[18] and generates a SOT[4]. The hurdle posed by this approach is that graphene shunts a substantial portion of the flowing current and therefore limits the torque efficiency. Therefore, an ideal solution would be to utilize an insulating material whose hybridization with the ferromagnetic orbitals would result in enhanced interfacial potential drop. Nonetheless, these two criteria, insulating bulk with strong interfacial hybridization, seem contradicting each other.

In this work, we demonstrate that an ideal compromise is realized by transferring h-BN onto $SrRuO_3$ (SRO), resulting in giant Rashba SOC and gate-controlled current-driven magnetization switching, the schematic illustration of which is shown in Fig. 1a. This result is surprising as insulating van der Waals materials such as h-BN are regarded as inert with respect to transport measurement and are also not expected to strongly hybridize with adjacent metals. In fact, our first principles calculations demonstrate that at the h-BN/SRO interface metal-induced gap states emerge close to Fermi level upon hybridization between p_z orbitals of h-BN and t_{2g} orbitals of SRO. The presence of these mid-gap states at the h-BN/SRO interface unlocks the gate voltage control of the REE splitting. The exotic role of the interface between h-BN and SRO is also distinguished by our control experiments on SRO single layer and the amorphous $LaAlO_3$ (LAO) inserted h-BN/LAO/SRO structure.

For the structure investigated in this report, an epitaxial SRO (6nm) was deposited onto the $SrTiO_3$ (STO) substrate with (110) crystallographic orientation by pulsed laser deposition (PLD). Then an exfoliated h-BN was transferred to the surface of the grown SRO thin film, whose optical image is shown in the insert of Fig. 1b. The Raman peak of the h-BN onto SRO is located at 1366 cm^{-1}, as shown in Fig. 1b, which is the same as the one exfoliated onto SiO_2. The Raman peak located at 1300 cm^{-1} for the h-BN/SRO structure is from the STO substrate. In order to get SRO films with perfect PMA property for the SOT device, the (110)-oriented

STO is chosen for the growth such that the magnetic easy axis of SRO (in the [010] lattice direction of the orthorhombic structure) will be aligned exactly along the out-of-plane (OOP) direction[19], which is verified by the X-ray diffraction (XRD) (see Fig. S1). The cross-sectional scanning transmission electron microscopy (STEM) was utilized to further characterize the quality of the h-BN/SRO structure (Fig. 1c). Good crystallinity of the epitaxial SRO thin film and a sharp SRO/STO interface can be confirmed from the high magnification high angle annular dark field (DF) and bright field (BF) images as shown in Fig. 1c(2) and Fig. 1c(3), respectively. Besides, the thickness of SRO (6 nm) is confirmed, and the layer structure of h-BN with a distance of 0.34 nm in the direction of *c* axis is clearly seen (Fig. 1c(4)). Finally, the magnetic measurements were performed to characterize the easy axis of the grown SRO $(110)_{pc}$ film, where pc subscript refers to pseudo-cubic. The temperature dependent magnetization of the SRO thin film along in-plane (IP) and OOP directions are shown in Fig. 1d. The negligible IP component of magnetization indicates the perfect PMA of the grown SRO thin film. This is further confirmed by the magnetic hysteresis loops under OOP and IP directions for SRO at 60 K (Fig. 1e), where the remnant magnetic moments at zero field are almost zero for both IP loops.

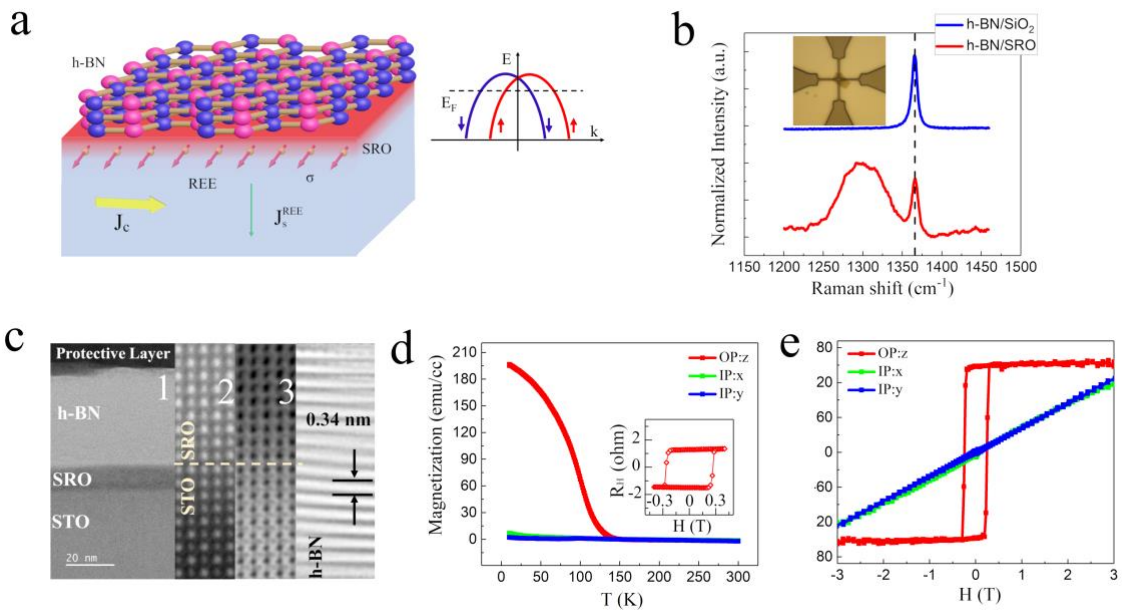

Figure1| Basic characterizations of the h-BN/$SrRuO_3$ structure. a, Schematic illustration of REE at h-BN/SRO interface (Inset shows the Rashba band dispersion). The yellow arrow represents the charge current, the green arrow represents the spin current and the pink arrows represent the spin polarization at the h-BN/$SrRuO_3$ interface. **b**, Raman spectra of the h-BN on SiO_2 and SRO at 300K, respectively. (Inset is the optical image of the h-BN/SRO structure with a cross-bar device) **c(1),** Low magnification BF STEM image of the sample cross-section. **c(2), c(3),** High magnification high angle annular DF and BF image of the SRO-STO interface. **c(4),** High magnification BF image of h-BN layers. **d**, Temperature dependent magnetization of SRO. For each M-T curve, the sample was cooled first from 300 K to 10 K under an external magnetic field of 40000 Oe, and then the magnetization was measured under zero magnetic field with the increasing temperature. Inset is the anomalous Hall effect (AHE) loop of h-BN/SRO at 60 K. **e**, Magnetic hysteresis loops of SRO at 60 K.

One of the main results in this study is that the current-induced magnetization switching is un-expectedly achieved in the h-BN/SRO$(110)_{pc}$ bilayer considering the insulating property

of h-BN, whose set-up is shown in Fig. 2a. Here, the Hall resistance is utilized as an indicator for the magnetization of the SRO layer and the measurement is performed at 60 K. Fig. 2b shows the current-induced magnetization switching (red curves) under a sweeping pulsed DC current and various external magnetic fields applied parallel to the DC current. One can see that a deterministic magnetization switching can be achieved with an external magnetic field applied, and the polarity of the switching loops changes when reversing the magnetic field from H_x=-1000 Oe to H_x=1000 Oe. Furthermore, the critical current for switching is found to decrease with increasing of the external magnetic field, as shown in Fig. 2c (the switching loops can be found in Fig. S2a). All these observations are consistent with the features of the SOT-induced magnetization switching[1,2]. Nevertheless, there are no conventional SOT sources in the h-BN/SRO bilayer structure. In order to distinguish the role of the h-BN in this structure, we fabricated two control devices, one is from the SRO single layer and the other from a structure with a LAO layer inserted between the h-BN and SRO layers. The LAO layer here is an insulator with a thickness of 2 nm and in-situ grew onto SRO. Both control devices show similar (AHE) loops at 60 K to that of h-BN/SRO bilayer (Fig. S2). However, neither of them presents the current-induced magnetization switching as the one from the h-BN/SRO device. The blue curves in Fig. 2b shows the result from the device based on h-BN/LAO/SRO, where no switching loops are observed whether there is an IP magnetic field or not. The switching result for the device of SRO single layer is shown in Fig. S3. Therefore, it can be inferred that the current-induced magnetization switching in h-BN/SRO device is strongly related to the interface between h-BN and SRO. It is noted that the switching ratio, defined as current-induced resistance change divided by AHE resistance, is below one hundred percent. The possible factors responsible for the partial magnetization switching is discussed in the section 4 of the Supplementary Material.

Next, we quantify the current-induced spin-orbit effective field in the h-BN/SRO bilayer by measuring the current-induced shift of the OOP hysteresis loop as functions of the IP bias magnetic field. Here, the quantified current-induced spin-orbit field refers to the damping-like spin orbit field, which is the driving source for the magnetization switching[10]. We do not use the conventional second harmonic Hall voltage method because it mixes with the signal from the thermoelectric effect (section 5 in the supplementary), which can be ruled out by the method used here[20]. Fig. 2d shows the AHE loops at $\pm$1.5mA under a bias IP magnetic field of 8.5 kOe. One can see that the AHE loops shift towards opposite directions under opposite DC current, indicating the existence of a current-induced effective field due to the SOT. The effective field H_{eff} can be extracted from the horizontal shift of the AHE loop under the DC current. Fig. 2e shows the summarized H_{eff}/J$_c$ as a function of the bias IP magnetic field along x direction, where J$_c$ is the current density. H_{eff}/J$_c$ increases linearly with H_x at first and saturates around 10 Oe/(10^7A/cm^2) when H_x is larger than 5000 Oe. These observations also suggest that the magnetization switching in the h-BN/SRO layers occurs through magnetic domain nucleation and expansion[21], which implies the presence of the Dzyaloshinskii-Moriya interaction (DMI) in the structure. In such a scenario, the IP field is to suppress the DMI effective field to achieve the domain expansion, i.e. assisting the magnetization to switch in SRO, as shown in Fig. 2b. Accordingly, the IP bias field, which corresponds to the saturated position of the H_{eff}/J$_c$, equals to the DMI field in the structure, i.e. DMI field in h-BN/SRO is about 5000 Oe. Furthermore, one can obtain that the damping-like spin-orbit effective field is the saturated value of 10 Oe/(10^7A/cm^2), which is comparable with the damping-like spin-orbit effective field observed in TmIG/Pt[22].

Consequently, we can evaluate the DMI exchange constant D, which is obtained from D=$\mu_0 M_s \Delta H_{DMI}$. Here Δ is domain wall width[22] and can be obtained from $\Delta = \sqrt{A/K_{u,eff}}$, where A is the exchange stiffness constant, $K_{u,eff}$ is the effective magnetic anisotropy energy.

Ms and $K_{u,eff}$ are 153 emu/cc and 2.7×10^6 erg/cc, respectively, derived from the measured M-H loop. Exchange stiffness constant A is assumed to be 2 pJ/m for SRO[23]. Then we obtain the DMI exchange constant D=0.21 mJ/m^2, which is comparable with the DMI exchange constant of Ta/CoFeB/MgO[20].

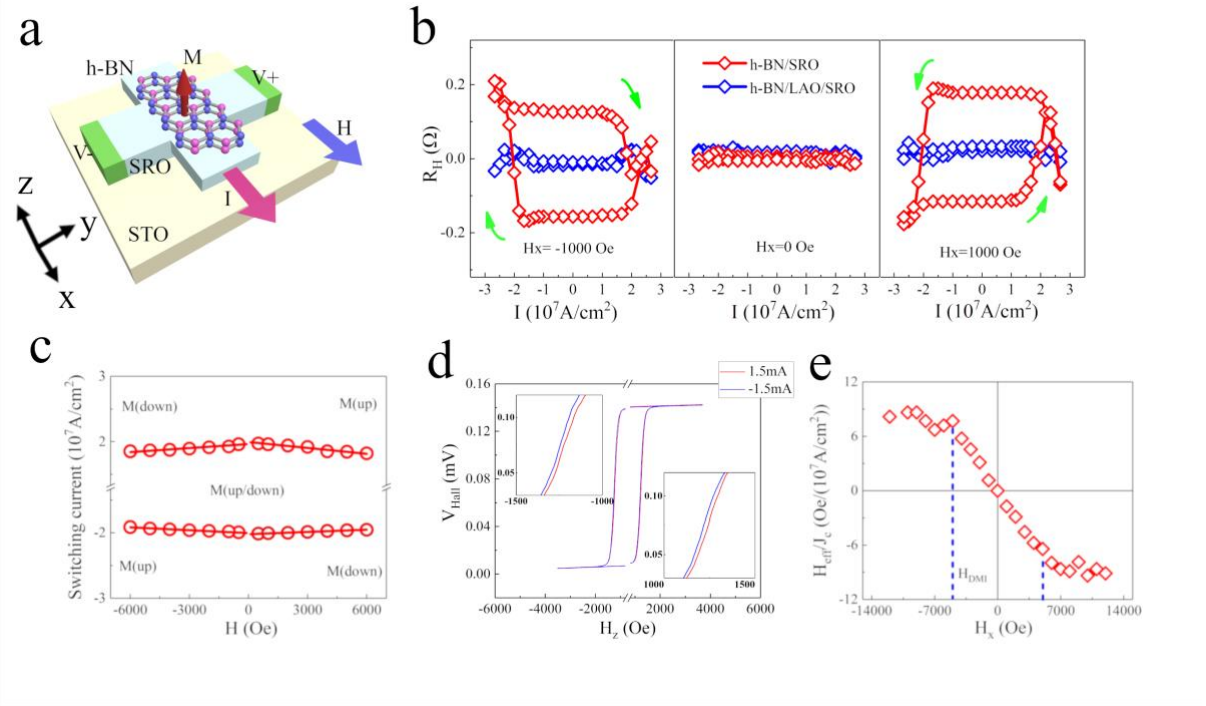

Figure 2 | Current-induced magnetization switching in h-BN/SRO bilayer. a, Schematic of the set-up for the devices based on the h-BN/SRO bilayer **b,** Current-induced magnetization switching in h-BN/SRO bilayer (red curves) when Hx=-1000 Oe, 0 Oe and 1000 Oe. Hx is along the current direction. Blue curves show the measurements from the control sample of h-BN/LAO/SRO. **c,** Switching phase diagram under the external magnetic field and DC current. **d,** Opposite shift of AHE loops at ±1.5mA under a bias IP magnetic field. Inserted images are the zoom-in area of the AHE loop varying from 1000 Oe (-1000 Oe) to 1500 Oe (-1500 Oe). **e,** Measured H_{eff} as a function of the bias IP magnetic fields.

Next, we would like to discuss the possible SOT origin in the h-BN/SRO bilayer. Generally, in the scenario of SOT-induced magnetization switching, SHE and REE are

recognized as the main mechanisms to generate the spin current to exert a torque onto magnetization. While SHE originates from the bulk SOC, the REE comes from the interfacial SOC. In the case of SHE, a spin current with transverse spin polarization is generated when a charge current passes through a heavy metal with strong SOC. In the h-BN/SRO structure, no current passes through the insulating h-BN layer. Therefore, SHE from the non-magnetic layer shall not exist in the h-BN/SRO bilayer due to the electric-insulating nature and weak SOC in h-BN. Thus, one may think that the spin Hall current arises from SRO itself. Recently, anomalous spin current sources have been reported to emerge in a magnetic single layer, for example, the SHE and AHE-induced spin currents[24]. However, the SHE-induced spin current would have opposite components in opposite directions that would cancel each other, while the AHE-induced spin current will have the same spin polarization direction as the magnetic moment of SRO, which cannot execute a torque on itself. These are further supported by the disappearance of the current-induced magnetization switching in the two control devices (one is with the SRO single layer, and the other with the h-BN/LAO/SRO structure). Therefore, it is reasonable to ascribe the origin of the SOT in the h-BN/SRO bilayer to the interface between h-BN and SRO layers.

The first-principles density functional theory (DFT) calculations were implemented to reveal the role of the h-BN/SRO interface in determining the current-induced SOT. Extended data Fig. 1a and 1b show the side and top views of the structure models of h-BN/SRO $(110)_{pc}$ for the calculations. In order to see the structure-contributed spin splitting (not Zeeman-type), the electronic band structures of h-BN/SRO $(110)_{pc}$ are calculated with the magnetization aligned along $[100]_o$ and $[\bar{1}00]_o$ directions (subscript o refers to orthorhombic), respectively, as shown by the black and red curves in Fig. 3a. One can see that the band structure of the h-BN/SRO $(110)_{pc}$ heterostructure presents characteristic Rashba-type splitting, and the splitting magnitude strongly depends on the position of the band. For example, considering the two

bands that intersect the Fermi level and have the lowest energy in Γ point, as shown in the zoom-in plot in Fig. 3a, one can see that a larger band splitting exists in the upper bands. To quantify the Rashba effect, Rashba coefficients of the two bands are extracted as $\alpha_1 = 2E_1/k_1$ and $\alpha_2 = 2E_2/k_2$ with E_1 = 0.001 meV and E_2 = 7.693 meV being the Rashba splittings at the wave vectors k_1 = 0.001 Å^{-1} and k_2 = 0.028 Å^{-1} for the two bands, respectively. E_1 and k_1 are not shown in Fig. 3a due to their small values. We find that although Rashba coefficient α_1 of the band nearest to the Fermi level is only 2 meV Å, the Rashba coefficient α_2 of the other band is as large as 550 meV Å, which is comparable to that of Au (111) (330 meV Å) [25] and Bi(111) (550 meV Å)[26] surfaces. In order to further shed light on the origin of the Rashba splitting at the h-BN/SRO interface, we calculated the density of states (DOS) of h-BN/SRO. From Fig. 3b, it can be identified that, for the h-BN, there are in-gap states at about -0.8 eV below the Fermi level (indicated by green arrow) due to the hybridization of Ru-3d and (B+N)-2p states. Those in-gap states are mostly contributed by the p_z orbitals of N atoms for both spin channels as shown in the top panel of Fig. 3c. It is noted that the in-gap states are strongly coupled to all the five Ru-3d orbitals for the spin-up channel, while it is only coupled to the dz^2, d_{xz}, and dx^2-y^2 orbitals for the spin-down channel from the bottom panel of Fig. 3c.

With the band structure information of the h-BN/SRO interface, we develop an effective tight-binding model to qualitatively describe how the interfacial hybridization induced in-gap state modify the SOT properties of h-BN/SRO. In such a model, which is described in detail in the method, the hybridization between the two layers is tuned by modifying the onsite energy detuning (ε_0) between h-BN and SRO. It is found that there is a strong resonance state around the Fermi level when ε_0 is in the range between $2.5t_1$ and $3t_1$, where t_1 is the in-plane orbital hopping matrix element in SRO. Three experimentally relevant quantities, the field-like torque, the damping-like torque and the DMI, are calculated under different onsite energy detuning. All these three quantities emerge from the combination of

magnetism, spin-orbit coupling and inversion symmetry breaking. Concretely, tuning ε_0 modifies the hybridization between the insulating and magnetic layers and thereby changes the interfacial potential gradient between them. Consequently, the two interfaces of the ferromagnetic layer become inequivalent, resulting in non-vanishing torques and DMI.

The dependence of the three spin-orbit properties as a function of ε_0 are reported on Fig. 3d, where the vertical dashed lines indicate selected remarkable situations. Away from the resonance range ($\varepsilon_0 < 2.5t_1$ and $\varepsilon_0 > 3t_1$), the calculated torques and DMI are small due to weak coupling between h-BN and SRO. Between these two detuning values, the three quantities display quite different behavior, illustrating their different microscopic physical origin: The field-like torque only involves intra-band transitions, whereas both the damping-like torque and DMI arise from inter-band transitions. The field-like torque reaches a maximum in the resonance region, which is reasonable since hybridization between the h-BN and SRO is maximized in this range and therefore the dissimilarity between the two ferromagnetic interfaces is optimized. The behavior of the damping-like torque and DMI is more intriguing and displays two main features: away from resonance (for $\varepsilon_0 < 2.5t_1$ and $\varepsilon_0 > 2.9t_1$), they both increase when tuning ε_0 towards resonance. In the resonance region through, these two quantities exhibit opposite behavior, that is DMI reaches a maximum while the damping-like torque vanishes (markers (1) and (3)) and vice-versa (marker (2)). This opposite behavior is likely to be related to the different energy dependence of the two physical properties, as displayed by the equations in method.

Although this effective model would not quantitatively describe the experimental observations, it does suggest that the measured spin-orbit field and DMI arise from the hybridization effect between SRO and h-BN, which thus results in the current-induced magnetization switching in SRO. Based on our DFT calculations, the mid-gap states of h-BN that drives the inversion symmetry breaking are located a few hundreds of meV away from

Fermi level so that the hybridization at h-BN/SRO interface is off-resonance, which will give rise to small but finite torques and DMI. As a result, it is expected that the spin-orbit field and DMI in the h-BN/SRO structure will be either enhanced or quenched with the change of the hybridization state via, for example, gating voltages in this off-resonance regime. So does the current-induced magnetization switching efficiency.

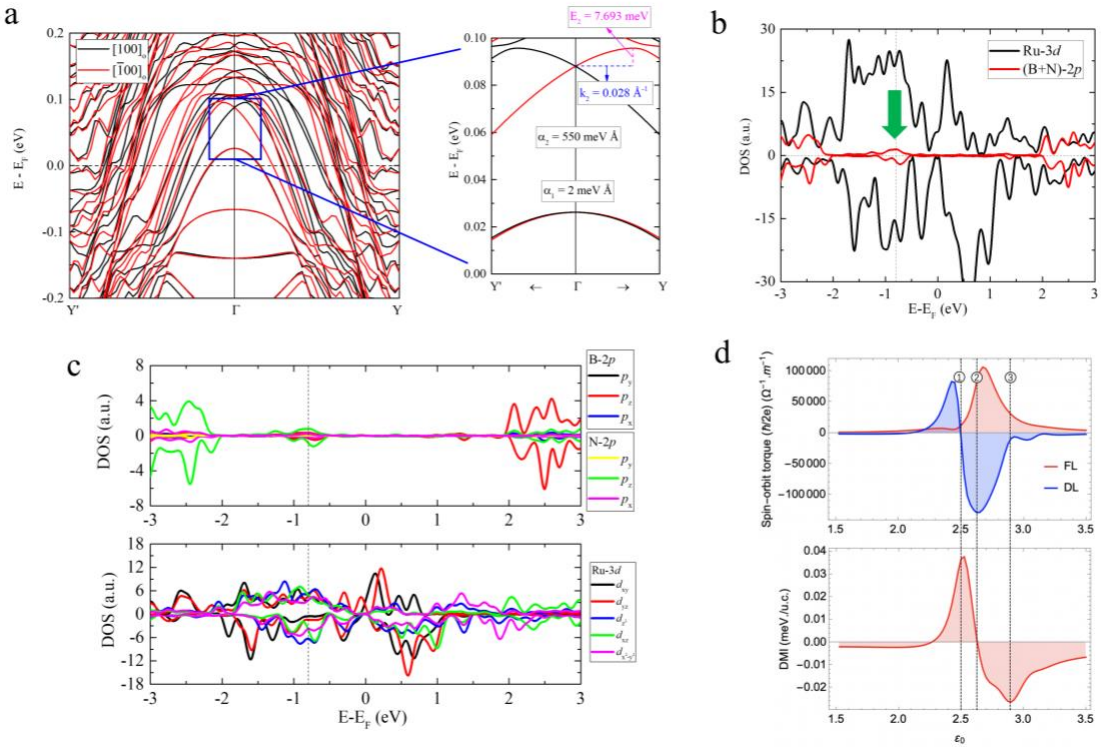

Figure 3|Microscopic origin of SOT at the h-BN/SRO interface. a, The calculated band structures of the h-BN/SRO $(110)_{pc}$ heterostructure with magnetization points along $[100]_o$ (black lines) and $[\bar{1}00]_o$ (red lines) directions. Zoom-in plot is the two bands that intersect the Fermi level and have the lowest energy in Γ point. **b,** DOS of (B+N)-2p and Ru-3d states. **c,** Detailed DOS of (B+N)-2p (top panel) and Ru-3d states (bottom panel). **d**, (Top panel) Field-like (red line), damping-like torque (blue line), and (bottom panel) DMI as a function of the detuning ε_0. The vertical dashed lines indicate three remarkable situations at resonance. FL refers to the field-like torque and DL refers to the damping-like torque.

Consequently, we employed an ionic-liquid gating experiment to investigate the electrostatic effect on the current-induced SOT and thus the magnetization switching. Fig. 4a shows the schematic set-up for the gating experiment. In this experiment, the transverse effective magnetic field (H_T) measured by the second harmonic Hall measurement is extracted to indicate the current-induced SOT, since the Hall voltage related to the longitudinal damping-like field contributing to the magnetization switching mixes strongly with the signal from the thermal effect (section 5 in the supplementary), and the current-induced shift of the OOP hysteresis loop as a function of the IP bias magnetic field is not able to be conducted in this set-up. During the measurement, a small AC current with a frequency of 13.7 Hz and an IP sweeping magnetic field within a small range are applied to the Hall bar device, and the resulted first harmonic voltage and second harmonic voltage are simultaneously probed by two lock-in amplifiers. Fig. S8 shows the second harmonic voltages $V_{2\omega}$ as a function of the transverse magnetic field under gating voltages ranging from -1 V to +2.5 V at 60 K , where "M+" and "M-" represent moment up and down in SRO, respectively. One can see that the slope of the second harmonic Hall voltage changes sign upon reversing the magnetic moment direction, consistent with the feature of the transverse field due to the odd SOT[27]. The transverse effective magnetic field H_T is obtained by $\{\frac{\partial V_{2w}}{\partial H} / \frac{\partial^2 V_w}{\partial H^2}\}_{H\|T.}$ It is estimated to be 198 Oe/(10^7A/cm^2) when the gate voltage is 0V, which is far larger than that extracted from the current-induced AHE shift as function of the IP bias magnetic field. Since the effective field from the latter method reflects the magnitude of the damping-like effective field for the magnetization switching while the former one for the field-like effective field, the large difference between these two fields is consistent with the feature of the current-induced SOT from REE[4]. Fig. 4b summarizes the extracted transverse effective magnetic field under various gate-voltages. One can see that the H_T increase as the gate-voltage increases, indicating a significant electrostatic effect.

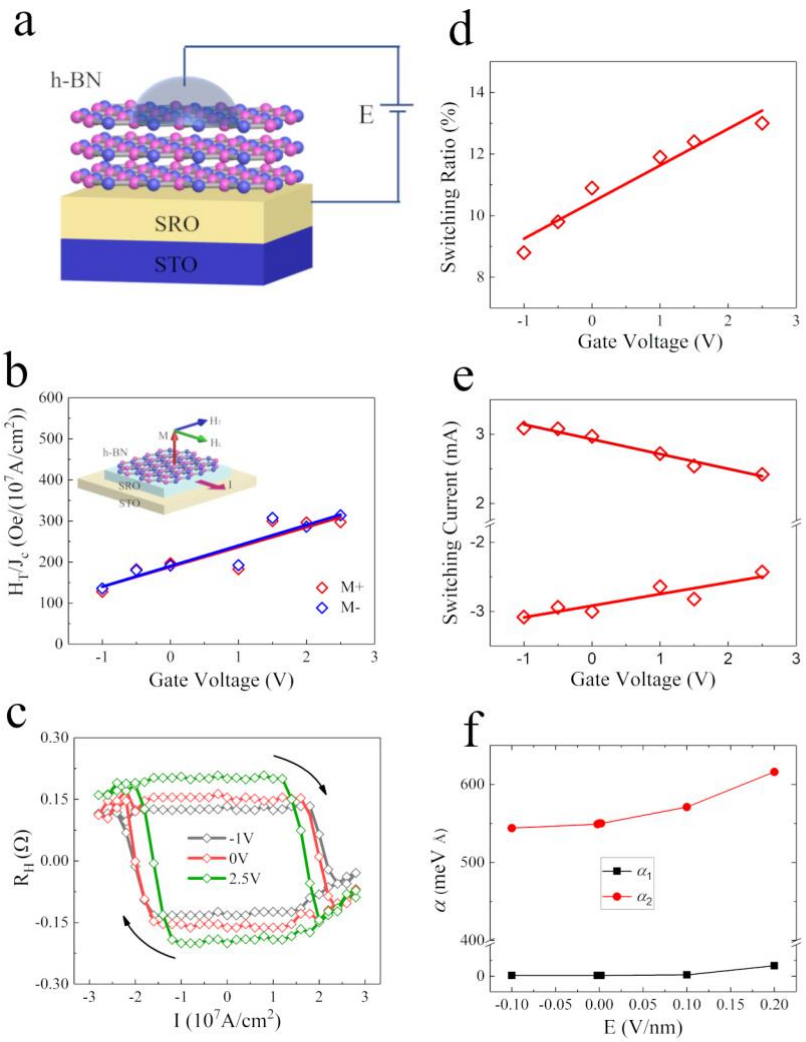

Figure 4| Gate-voltage tunable effective magnetic field and current-induced magnetization switching. a, Schematic set-up of the ionic-liquid gating experiment on the h-BN/SRO structure. **b,** Transverse spin-orbit effective field for M± as a function of the gate-voltage. The applied AC current is 1.5 mA and inserted image is the schematic set-up for the harmonic Hall voltage measurement. **c,** Current-induced magnetization switching loops under different gate-voltages. Here, the external magnetic field is fixed to be -2000 Oe and parallel to the applied pulsed current. Black arrow represents the switching polarity. **d, e,** Gate-voltage dependence of the switching ratio (**d**) and critical switching current (**e**). **f,** The calculated

electric field dependent Rashba coefficients of the h-BN/SRO heterostructure. The solid curves in the figures are eye-guides for the data.

Fig. 4c shows the current-induced magnetization switching loops under -1 V, 0 V and +2.5 V of the gate-voltage, where the critical switching current and the switching loops are modulated obviously. Fig. 4d and Fig. 4e plot the extracted magnetization switching ratios and critical currents as functions of gate-voltages, respectively. One can see that the switching ratio increases upon the gate-voltage varying from -1 V to +2.5 V, while the critical current decreases upon the gate-voltages. These observations indicate that the gate-voltage can undeniably enhance the current-induced switching efficiency in h-BN/SRO structures. Such a trend, as well as that of the extracted field-like effective field, is consistent with the off-resonance scenario inferred from the tight-binding model, i.e. the gate-voltage modulates the torques and DMI induced by the hybridization state at the h-BN/SRO interface. Furthermore, we also calculate the electric field dependence of the Rashba coefficients as shown in the Fig. 4f, which are extracted from the calculated band structures (Fig. 3a) from first-principles calculations (Methods). It is found that the Rashba coefficient can be effectively tuned by the electric field. In particular, the electric field of 0.2 V/nm can further enhance the Rashba coefficients α_1 and α_2 up to 33 and 616 meV Å, respectively. The modulation of the Rashba effect by the gate-voltage is consistent with the enhanced hybridization effect at the h-BN/SRO, which results in inequivalent interfaces on two sides of SRO. During the gating experiment, the AHEs under different gate-voltages were measured too (Fig. S9). They show almost the same shape under different gate-voltages, which hints that the trivial gating effect on the magnetic property of SRO does not contribute to the tuning effect on the current-induced SOT and magnetization switching.

In conclusion, current-induced REE-SOT and magnetization switching are demonstrated in a bilayer structure with vdW interface between the insulating h-BN and

perpendicularly magnetized SRO $(110)_{pc}$. These observed phenomena are ascribed to the Rashba effect induced at the interface between h-BN and SRO, which is confirmed by the first-principles calculations. A simplified tight-binding model is employed to explain how the SOTs and DMI are generated in such an asymmetric h-BN/SRO bilayer, which is further supported by the evident electrostatic effect on the current-induced SOT and magnetization switching. The exotic properties induced by the insulating h-BN reported here also remind the 2D materials community to be careful with the hidden role the h-BN may play in studies of the novel properties of the van der Waals materials, where the h-BN is widely used as an inert protection layer.

Methods:

Sample preparation: SRO thin films were deposited by PLD with laser wavelength of 248 nm. The base pressure of the chamber for growth SRO was 5×10^{-7} torr. The growth parameters were optimized as following: the energy density of laser was 1.5 J/cm^2, the substrate was heated up to 750^{o}C and oxygen pressure was set to 20 mtorr during growth. After the SRO thin films were prepared well, h-BN was exfoliated from single crystals and then transferred onto SRO.

Characterizations: Raman spectrum was measured by a Thermo Scientific DXR Raman microscope with a 514 nm excitation and a 100X objective. Magnetic properties were measured by SQUID (Quantum design MPMS3). Cross-sectional STEM was carried out in a JEOL ARM200F atomic resolution electron microscope equipped with cold field emission gun, an ASCOR 5th order aberration corrector.

Device fabrication and transport measurement: The h-BN/SRO was patterned into cross bar with a width of 2.5 μm by laser writer and ion milling. The magnetization switching and harmonic Hall measurements were conducted in PPMS. A Keithley source meter 6221 and

lock-in-amplifiers were employed for the switching and harmonic Hall measurement. The current-induced shifts of the OOP hysteresis loop as function of the IP bias magnetic field were measured by a SOT magnetometry method via accessing a Cryogenic triple-axis superconducting magnet (5T-2T-2T).

Rashba splitting and DOS calculations: The first-principles calculation were performed within the framework of density functional theory (DFT) as implemented in the Vienna ab-initio simulation package (VASP)[28]. The electron-core interactions are described by the projector augmented wave method[29] and the exchange correlation energy are calculated within the generalized gradient approximation of the Perdew-Burke-Ernzerhof (PBE) form[30]. In addition, we include on-site Coulomb interaction with U = 1.4 and J = 0.4 eV for the Ru d states. To reduce the lattice mismatch between SRO $(110)_{pc}$ and h-BN, we have considered a large h-BN/SRO$(110)_{pc}$ heterostructure consisting of $4\sqrt{3}\times3$ unit cell of h-BN monolayer and 3×2 SRO$(110)_{pc}$ surface unit cell with three Sr-Ru-O layers. We use an energy cutoff of 500 eV and k-point sampling on a Γ-centered 2×1×1 k-point mesh for the system. Extended data figure 1a and 1b show the side and top views of relaxed crystal structure of h-BN/SRO$(110)_{pc}$ heterostructure with the forces on each atom are smaller than 0.001 eV/Å. We find that average distance between h-BN and SRO$(110)_{pc}$ surface is 3 Å, and, more importantly, both the structures of h-BN and SRO$(110)_{pc}$ are distorted due to their interlayer interaction. Next, to extract the Rashba coefficient, we solve the Kohn-Sham equations with no SOC taken into consideration to determine the charge distribution and the DOS for ground state of the relaxed structure. Then SOC is included and the electronic band structures of system are determined when the magnetization points along the opposite $[100]_o$ and $[\bar{1}00]_o$ directions, respectively. The dipole moment correction is considered in the calculations of the electric field dependence of the band structure.

Tight-binding model of SOT and DMI: We develop an effective tight-binding model that qualitatively describes the modification of the spin-orbit properties of h-BN/SRO upon modifying the interfacial hybridization between the two layers. In fact, the large lattice mismatch between h-BN and SRO and the resulting large supercell required to model the band structure of the bilayer impedes the use of Wannier interpolation procedure. Therefore, we opt for an effective tight-binding model that comprises the following key ingredients: (i) the SRO magnetic layer is modeled by an undistorted cubic structure with t_{2g} orbitals and possessing atomic spin-orbit coupling; (ii) the insulating h-BN is modeled by a cubic bipartite lattice whose lattice parameter matches that of the magnetic layer; (iii) the hybridization between the two layers is tuned by modifying the onsite energy detuning between the two layers. Notice that because of the perfect lattice matching in our model, no mid-gap states emerge upon interfacial hybridization. To uncover the relation between interfacial potential drop and spin-orbit properties, we focus on the region of parameters where the Fermi level is close to the valence band, a situation that features qualitatively similar physics.

The magnetic layer is modeled based on the effective undistorted cubic SRO structure proposed in Reference 31[31]. In the $\{d_{yz}, d_{xz}, d_{xy}\}$ basis, it reads:

$$H_{\mathrm{SRO}} = \begin{pmatrix} \varepsilon_{yz} - \Delta\sigma_z & f_{yz,xz} & f_{yz,xy} \\ f_{yz,xz} & \varepsilon_{xz} - \Delta\sigma_z & f_{xz,xy} \\ f_{yz,xy} & f_{xz,xy} & \varepsilon_{xy} - \Delta\sigma_z \end{pmatrix} + i\lambda\epsilon_{abc}\sigma_c$$

$$\varepsilon_{yz} = -2t_1(\cos k_y + \cos k_z) - 2t_2 \cos k_x$$
$$\varepsilon_{xz} = -2t_1(\cos k_x + \cos k_z) - 2t_2 \cos k_y$$
$$\varepsilon_{xy} = -2t_1(\cos k_x + \cos k_y) - 2t_2 \cos k_z$$
$$f_{ab} = -4f \sin k_a \sin k_b$$

Since we do not intend to quantitatively describe the actual band structure of SRO, we simply adopt the parameters of Reference 31[31], given in the table below. In the following, H_{SRO} is discretized along z in order to build a N-layer slab, as depicted on extended data figure 2:

$$H_{\mathrm{SRO}} \to H_{slab} = \begin{pmatrix} H_L & H_T & 0 \\ H_T^\dagger & \ddots & H_T \\ 0 & H_T^\dagger & H_L \end{pmatrix}$$

, where H_L is the Hamiltonian of the square lattice in the (x,y) plane and H_T is the hopping matrix along z.

SrRuO₃ parameters (a=3.93A in the undistorted cubic structure)				
t_1	t_2	f	Δ	λ
1	-0.2	0.2	1	0.4

Based on the density functional theory calculations, h-BN hybridizes with SRO through its p_z orbitals. In our model, we consider a (checkerboard) bipartite square lattice with p_z orbitals only. In the sublattice representation, the Hamiltonian reads:

$$H_{\mathrm{I}} = \begin{pmatrix} \varepsilon_A & t_z(\cos k_x + \cos k_y) \\ t_z(\cos k_x + \cos k_y) & \varepsilon_B \end{pmatrix}$$

Here t_z is the π-hopping integral between p_z orbitals, and $\varepsilon_{A,B}$ are the onsite energies of the two sublattices. In our model, we take $t_z = 0.5$ and $\varepsilon_{A,B} = \varepsilon_0 \pm \frac{\varepsilon_g}{2}$, where $\varepsilon_g = 5$ is the insulating gap and ε_0 is the energy detuning of the insulating states with respect to the ferromagnetic ones.

The coupling between the $\{d_{yz}, d_{xz}, d_{xy}\}$ orbitals of the ferromagnetic layer and the p_z of the insulating layer is parameterized using Slater-Koster scheme[32]. The interlayer coupling reads:

$$H_{hyb} = \begin{pmatrix} T_{yz}^A & T_{yz}^B \\ T_{zx}^A & T_{zx}^B \\ T_{xy}^A & T_{xy}^B \end{pmatrix}$$

,where T_γ^α represents the hopping integral between the p_z orbital of sublattice α and the d_γ orbital of the magnetic lattice. Explicitly,

$$T_{yz}^A = -\frac{2i}{\sqrt{3}}\left(\frac{1}{\sqrt{3}}V_\sigma + \frac{1}{3}V_\pi\right)\sin\frac{(k_x - k_y)}{2} \qquad T_{yz}^B = \frac{2i}{\sqrt{3}}\left(\frac{1}{\sqrt{3}}V_\sigma + \frac{1}{3}V_\pi\right)\sin\frac{(k_x + k_y)}{2}$$

$$T_{zx}^A = \frac{2i}{\sqrt{3}}\left(\frac{1}{\sqrt{3}}V_\sigma + \frac{1}{3}V_\pi\right)\sin\frac{(k_x - k_y)}{2} \qquad T_{zx}^B = \frac{2i}{\sqrt{3}}\left(\frac{1}{\sqrt{3}}V_\sigma + \frac{1}{3}V_\pi\right)\sin\frac{(k_x + k_y)}{2}$$

$T_{xy}^{A} = -\frac{2}{\sqrt{3}^3}\left(\sqrt{3}V_\sigma - 2V_\pi\right)\cos\frac{(k_x-k_y)}{2}$ $\qquad$ $T_{xy}^{B} = \frac{2}{\sqrt{3}^3}\left(\sqrt{3}V_\sigma - 2V_\pi\right)\cos\frac{(k_x+k_y)}{2}$

V_σ and V_π are the p-d Slater-Koster parameters that we fix to $V_\sigma = 0.1$ and $V_\pi = -0.05$.

Our intention is to understand how the spin-orbit coupling properties are modified when tuning the hybridization between the ferromagnet and the insulating substrate. We will particularly focus on the longitudinal conductivity, σ_L, the field-like and damping-like SOT, $\boldsymbol{T}_{FL}$ and $\boldsymbol{T}_{DL}$, and the DMI. These quantities are computing using Kubo linear response[33,34]:

$$\sigma_L = \frac{e\hbar}{4\pi a}\int d\varepsilon \partial_\varepsilon f(\varepsilon)\mathrm{Tr}[(G^R - G^A)\hat{v}_x(G^R - G^A)\hat{v}_x]$$

$$\boldsymbol{T}_{FL} = \frac{\hbar}{4\pi}\int d\varepsilon \partial_\varepsilon f(\varepsilon)\mathrm{Tr}\left[(G^R - G^A)(e\boldsymbol{E}\cdot\hat{\boldsymbol{v}})(G^R - G^A)\hat{\boldsymbol{T}}\right]$$

$$\boldsymbol{T}_{DL} = \frac{\hbar}{4\pi}\int d\varepsilon f(\varepsilon)\mathrm{Tr}\left[(G^R - G^A)(e\boldsymbol{E}\cdot\hat{\boldsymbol{v}})(\partial_\varepsilon G^R + \partial_\varepsilon G^A)\hat{\boldsymbol{T}}\right]$$

$$D_{ij} = \frac{\hbar}{2\pi}\mathrm{Re}\int d\varepsilon(\varepsilon - \varepsilon_F)f(\varepsilon)\mathrm{Tr}\left[\left(\partial_\varepsilon G^R \hat{v}_j G^R - G^R \hat{v}_j \partial_\varepsilon G^R\right)\hat{T}_i\right]$$

Here, $G^{R,A} = (\varepsilon - H \pm i\Gamma)^{-1}$ are the retarded and advanced Green functions, $\hat{\boldsymbol{v}} = \partial_{\hbar\boldsymbol{k}}H$ is the velocity operator and $\hat{\boldsymbol{T}} = \Delta\mathbf{z}\times\hat{\boldsymbol{\sigma}}$ is the torque operator[33,34] σ_L is expressed in $\Omega^{-1}\cdot m^{-1}$, $\boldsymbol{T}_{FL}$ and $\boldsymbol{T}_{DL}$ are normalized to the electric field and expressed in $\left(\frac{\hbar}{2e}\right)\Omega^{-1}\cdot m^{-1}$ and the DM tensor element, D_{ij}, defined as $\boldsymbol{D}\cdot(\boldsymbol{m}\times\partial_j\boldsymbol{m})$ is expressed in meV $\cdot$ Å per unit cell. In the calculations, we apply the electric field along x and take N=3.

The density of states of our bilayer is reported on extended data figure 3 projected on the magnetic layer (blue) and on the insulator orbitals (red). In this configuration, we set $\varepsilon_0 = 0$, so that the peaks of the valence and conduction bands of the insulator are symmetrically positioned with respect to the center of the ferromagnetic band width.

We first compute the longitudinal conductivity as a function of the parameter ε_0 at $\varepsilon_F = 0$. The results are displayed in extended data figure 3. The bottom panel shows the conductivity

as a function of ε_0. As a reference, we also report the layer-projected density of states for three selected detuning. It is clear that the resonance occurs around $\varepsilon_0 \approx 2.5t_1$, which corresponds to a sharp modification of the conductivity.

Acknowledgment:

The research is supported by the Singapore National Research Foundation under CRP Award No. NRF-CRP10-2012-02 and the Singapore Ministry of Education MOE2018-T2-1-019, MOE2018-T2-2-043, MOE2019-T2-2-075, A*STAR Grant No. A1983C0036, A*STAR IAF-ICP 11801E0036, MOE Tier1 R-284-000-195-114.

Author contributions: Q.X., W.L. and J.S.C. conceived and designed the experiments. J.L. and H.Y. conducted the first-principles calculations. A. M. developed the tight-binding model. Q.X., W.L., H.Z., X.L., H. C., X.S., L.L., S.C., C.H.Z., J.W.C., P.Y., K.P.L., W.J., performed the sample fabrications and experimental measurements. Q.X. and W.L. conducted the transport measurement. H.Z., W.J., performed the anomalous Hall resistance shift experiment. M.W. and J.W. performed the STEM. Q.X., W.L. and J.S.C. wrote the manuscript and all authors contributed to the final version.

Competing financial interests' statement

The authors declare no competing financial interests.

Reference:

1. Liu, L., Lee, O. J., Gudmundsen, T. J., Ralph, D. C. & Buhrman, R. A. Current-induced switching of perpendicularly magnetized magnetic layers using spin torque from the spin hall effect. *Phys. Rev. Lett.* **109**, 1–5 (2012).

2. Miron, I. M. *et al.* Perpendicular switching of a single ferromagnetic layer induced by in-plane current injection. *Nature* **476**, 189–193 (2011).

3. Sinova, J., Valenzuela, S. O., Wunderlich, J., Back, C. H. & Jungwirth, T. Spin Hall effects. *Rev. Mod. Phys.* **87**, 1213–1260 (2015).

4. Manchon, A., Koo, H. C., Nitta, J., Frolov, S. M. & Duine, R. A. New perspectives for Rashba spin-orbit coupling. *Nat. Mater.* **14**, 871–882 (2015).

5. Noël, P. *et al.* Non-volatile electric control of spin–charge conversion in a SrTiO3 Rashba system. *Nature* **580**, 483–486 (2020).

6. Lesne, E. *et al.* Highly efficient and tunable spin-to-charge conversion through Rashba coupling at oxide interfaces. *Nat. Mater.* **15**, 1261–1266 (2016).

7. Chen, L. *et al.* Electric-field control of interfacial spin-orbit fields. *Nat. Electron.* **1**, 350–355 (2018).

8. Liu, R. H., Lim, W. L. & Urazhdin, S. Control of current-induced spin-orbit effects in a ferromagnetic heterostructure by electric field. *Phys. Rev. B - Condens. Matter Mater. Phys.* **89**, 1–5 (2014).

9. Mishra, R. *et al.* Electric-field control of spin accumulation direction for spin-orbit torques. *Nat. Commun.* **10**, 1–8 (2019).

10. Lin, W. *et al.* Tuning of current-induced effective magnetic field through Rashba effect engineering in hybrid multiferroic structures. *NPG Asia Mater.* 740–748 (2018).

doi:10.1038/s41427-018-0069-7

11. Fang, M. *et al.* Tuning the interfacial spin-orbit coupling with ferroelectricity. *Nat. Commun.* **11**, 1–8 (2020).

12. Liu, L. *et al.* Spin-torque switching with the giant spin hall effect of tantalum. *Science (80-.).* **336**, 555–558 (2012).

13. Pai, C. F. *et al.* Spin transfer torque devices utilizing the giant spin Hall effect of tungsten. *Appl. Phys. Lett.* **101**, 1–5 (2012).

14. MacNeill, D. *et al.* Control of spin-orbit torques through crystal symmetry in WTe2/ferromagnet bilayers. *Nat. Phys.* **13**, 300–305 (2017).

15. Xie, Q. *et al.* Giant Enhancements of Perpendicular Magnetic Anisotropy and Spin-Orbit Torque by a MoS2 Layer. *Adv. Mater.* **31**, 1–9 (2019).

16. Song, P. *et al.* Coexistence of large conventional and planar spin Hall effect with long spin diffusion length in a low-symmetry semimetal at room temperature. *Nat. Mater.* 1–18 (2020). doi:10.1038/s41563-019-0600-4

17. Dc, M. *et al.* Room-temperature high spin–orbit torque due to quantum confinement in sputtered BixSe(1–x)films. *Nat. Mater.* **17**, 800–807 (2018).

18. Yang, H. *et al.* at graphene – ferromagnet interfaces due to the Rashba effect. *Nat. Mater.* **17**, (2018).

19. Liu, L. *et al.* Current-induced magnetization switching in all-oxide heterostructures. *Nat. Nanotechnol.* **14**, (2019).

20. Pai, C. F., Mann, M., Tan, A. J. & Beach, G. S. D. Determination of spin torque efficiencies in heterostructures with perpendicular magnetic anisotropy. *Phys. Rev. B* **93**, 1–7 (2016).

21. Baumgartner, M. *et al.* Spatially and time-resolved magnetization dynamics driven by spin-orbit torques. *Nat. Nanotechnol.* **12**, 980–986 (2017).

22. Avci, C. O. *et al.* Current-induced switching in a magnetic insulator. *Nat. Mater.* **16**, 309–314 (2017).

23. Ziese, M., Vrejoiu, I. & Hesse, D. Inverted hysteresis and giant exchange bias in La0.7 Sr 0.3 MnO3/SrRuO3 superlattices. *Appl. Phys. Lett.* **97**, 3–6 (2010).

24. Wang, W. *et al.* Anomalous spin–orbit torques in magnetic single-layer films. *Nat. Nanotechnol.* **14**, 819–824 (2019).

25. LaShell, S., McDougall, B. A. & Jensen, E. Spin splitting of an Au(111) surface state band observed with angle resolved photoelectron spectroscopy. *Phys. Rev. Lett.* **77**, 3419–3422 (1996).

26. Koroteev, Y. M. *et al.* Strong spin-orbit splitting on Bi surfaces. *Phys. Rev. Lett.* **93**, 1–4 (2004).

27. Manchon, A. *et al.* Current-induced spin-orbit torques in ferromagnetic and antiferromagnetic systems. *Rev. Mod. Phys.* **91**, (2019).

28. Kresse, G. & Furthmüller, J. Efficient iterative schemes for ab initio total-energy calculations using a plane-wave basis set. *Phys. Rev. B - Condens. Matter Mater. Phys.* **54**, 11169–11186 (1996).

29. Kresse, G. & Furthmüller, J. Efficiency of ab-initio total energy calculations for metals and semiconductors using a plane-wave basis set. *Comput. Mater. Sci.* **6**, 15–50 (1996).

30. Perdew, J. P., Burke, K. & Ernzerhof, M. Generalized gradient approximation made simple. *Phys. Rev. Lett.* **77**, 3865–3868 (1996).

31. Chen, Y., Bergman, D. L. & Burkov, A. A. Weyl fermions and the anomalous Hall effect in metallic ferromagnets. *Phys. Rev. B - Condens. Matter Mater. Phys.* **88**, 2–6 (2013).

32. Slater, J. C. & Koster, G. F. Simplified LCAO method for the periodic potential problem. *Phys. Rev.* **94**, 1498–1524 (1954).

33. Bonbien, V. & Manchon, A. Symmetrized decomposition of the Kubo-Bastin formula. *Phys. Rev. B* **102**, 85113 (2020).

34. Hajr, A., Hariri, A., Manchon, G., Ghosh, S. & Manchon, A. Semirealistic tight-binding model for Dzyaloshinskii-Moriya interaction. *Phys. Rev. B* **102**, 1–11 (2020).

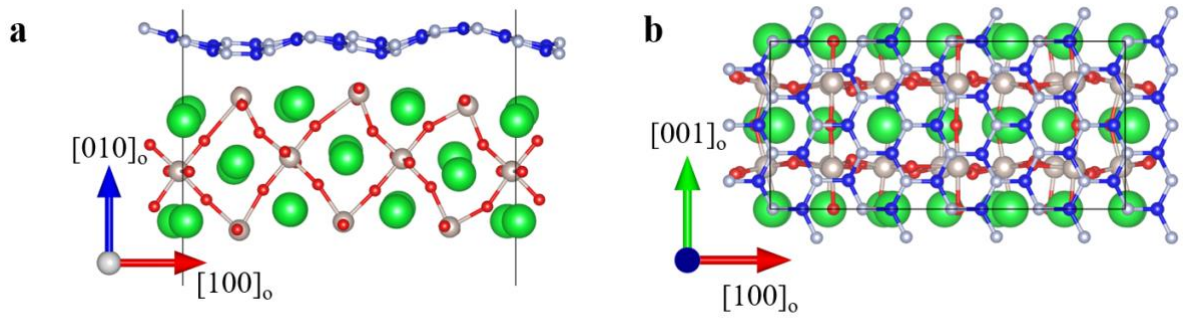

Extended data figure 1: Side (a) and top (b) views of relaxed crystal structure for the h-BN/SRO (110)pc heterostructure. Sr, Ru, O, B and N atoms are shown as green, grey, red, blue and white balls, respectively.

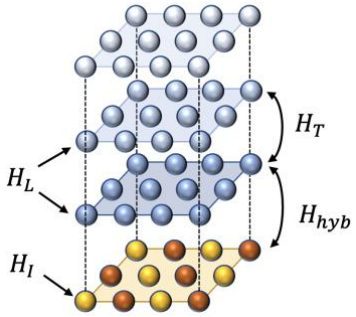

Extended data figure 2: Schematics of the heterostructure. The bottom layer represents the checkerboard insulator, where the yellow and brown spheres stand for the two sublattices and the top layers represent the cubic ferromagnet.

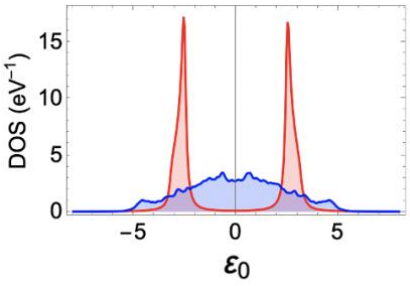

Extended data figure 3: Density of states projected on the magnetic layer (blue) and on the insulator orbitals (red) for $\varepsilon_0 = 0$.

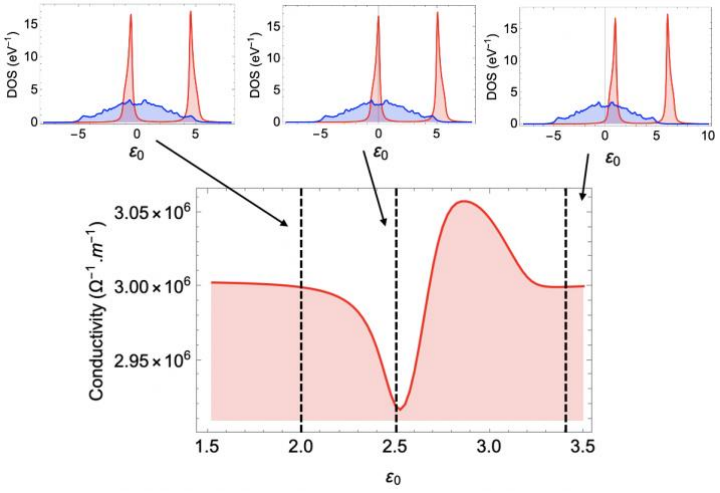

Extended data figure 4: Longitudinal conductivity as a function of the detuning ε_0. The vertical dashed lines indicate three remarkable situations whose corresponding density of states are represented on the top panel.